Impacts of the January 2022 Tonga volcanic eruption on the ionospheric dynamo: ICON-MIGHTI and Swarm observations of extreme neutral winds and currents

Brian J. Harding[1], Yen-Jung Joanne Wu[1], Patrick Alken[2], Yosuke Yamazaki[3], Colin C. Triplett[1], Thomas J. Immel[1], L. Claire Gasque[1], Stephen B. Mende[1], Chao Xiong[4]

[1]Space Sciences Laboratory, University of California Berkeley, Berkeley, CA, USA
[2]University of Colorado, Boulder, CO, USA
[3]GFZ German Research Centre for Geosciences, Potsdam, Germany
[4]Department of Space Physics, Electronic Information School, Wuhan University, 430072 Wuhan, China

Key Points:

- Extreme thermospheric winds and ionospheric currents were observed in coordinated space/ground-based measurements, ten hours post-eruption
- The westward electrojet current when the Lamb wave reaches the dayside is consistent with recent studies of the wind-driven electrojet
- Observations of linked dynamo processes provide direct evidence of the space-weather impacts of acute lower atmospheric forcing

Corresponding author: Brian J. Harding, `bharding@ssl.berkeley.edu`

Abstract

The eruption of the Hunga Tonga-Hunga Ha'apai volcano on 15 January 2022 triggered atmospheric waves at all altitudes. The NASA Ionospheric Connection Explorer (ICON) and ESA Swarm satellites were well placed to observe its impact on the ionospheric wind dynamo. After the Lamb wave entered the dayside, Swarm A observed an eastward and then westward equatorial electrojet (EEJ) on two consecutive orbits, each with magnitudes exceeding the 99.9th percentile of typically observed values. ICON simultaneously observed the neutral wind (90–300 km altitude) at approximately the same distance from Tonga. The observed neutral winds were also extreme (>99.9th percentile at some altitudes). The covariation of EEJ and winds is consistent with recent theoretical and observational results, indicating that the westward electrojet is driven by strong westward winds in the Pedersen region (∼120–150 km). These observations imply that the dynamo is a key mechanism in the ionospheric response to the Tonga disturbance.

Plain Language Summary

The January 2022 Tonga volcanic eruption caused atmospheric impacts around the world. As a natural experiment, it can be used to test our understanding of how the lower atmosphere affects space weather. Researchers are only beginning to document the chain of events post-eruption, and this paper focuses on its impact on the generator that drives electric fields in near-Earth space, a key part of space weather. This generator is driven by the atmosphere pushing charged particles across Earth's magnetic field. This usually creates a strong eastward current above the equator. When the Swarm A satellite coincided with the wave from Tonga, it observed that this current strengthened dramatically, then reversed. Although reversals are not unusual, this was the strongest reversal observed by Swarm since its 2013 launch, except for one large geomagnetic storm in 2015. Another satellite, the Ionospheric Connection Explorer, was luckily at the right time and place to observe related motions of the upper atmosphere, which were similarly extreme. These observations are shown to be consistent with our theoretical understanding of the generator. This study is important because it represents a critical test of atmosphere-space interactions and implies that the Tonga eruption caused a major space weather event.

1 Introduction

Isolated disturbances such as earthquakes, tsunamis, and solar eclipses, as well as explosions from volcanoes, nuclear detonations, and meteor air bursts can offer discrete tests for models of atmosphere-ionosphere coupling and variability (Aryal et al., 2020; Astafyeva, 2019; Inchin, Snively, et al., 2020; Li et al., 2021; Zettergren & Snively, 2019). The Hunga Tonga-Hunga Ha'apai (hereafter Tonga) volcanic eruption on 15 Jan 2022 generated atmospheric disturbances from the ground to the ionosphere (Adam, 2022; Wright et al., 2022). A typical wave mode excited by impulsive events in the lower atmosphere is the Lamb wave, an acoustic nondispersive edge wave (Garrett, 1969; Bretherton, 1969; Nishida et al., 2014). The study by Wright et al. (2022) presented data from the troposphere, stratosphere, and mesosphere, showing a coherent wave propagating at 318 m/s around the globe multiple times, identified as a Lamb wave. Although the Lamb wave propagates in the troposphere, energy leaks into higher altitudes, exciting other wave modes, in which the amplitude of wind, temperature, and pressure fluctuations can grow with altitude (Nishida et al., 2014; Wright et al., 2022). As such, the ionosphere, readily observed by ground-based instruments, can function as a sensitive monitor of atmospheric disturbances.

Indeed, initial Total Electron Content (TEC) observations have reported Traveling Ionospheric Disturbances (TIDs) propagating globally for many hours and even days

after the Tonga eruption (Aa et al., 2022; Lin et al., 2022; Themens et al., 2022; Zhang et al., 2022). Estimates of the horizontal wavelength of TIDs in the far field (i.e., at distances >3000 km from the eruption) range from 300 to 1000 km (Wright et al., 2022; Zhang et al., 2022). Additionally, Soares et al. (2022) reported oscillations of the geomagnetic field observed by a ground-based magnetometer 835 km from Tonga, which are attributed to short-period modulation (3-5 min) of ionospheric currents. No studies have yet reported data connecting the homosphere with these ionospheric signatures. Wright et al. (2022) presented ionospheric TIDs with phase speeds, horizontal wavelengths, and arrival times inconsistent with the Lamb wave, speculating that the observed TEC signatures likely arrived by indirect paths from Tonga.

The mechanisms through which signals from the lower atmosphere are transmitted and create observable effects in the ionosphere are numerous, and understanding their complex interplay is critical for interpreting and predicting ionospheric signals. These mechanisms include those resulting from direct propagation of the wave or waves to ionospheric F-region heights, modifying ion drag and/or plasma loss rates. Another mechanism is indirect, mediated by electric fields resulting from the neutral wind dynamo, which can carry signatures along magnetic field lines from the E region to the F region. The signal can also be transmitted to the opposite hemisphere, which has been proposed to explain the appearance of TIDs over Japan ahead of the Lamb wave (Lin et al., 2022). Conjugate effects were also suggested by Themens et al. (2022). In this study we report on two aspects of the Tonga disturbance: neutral winds and ionospheric dynamo signatures.

Specifically, we report extreme perturbations in the equatorial electrojet (EEJ) observed by Swarm and extreme perturbations in neutral winds from 90 to 300 km altitude observed by the Michelson Interferometer for Global High-resolution Thermospheric Imaging (MIGHTI) on the Ionospheric Connection Explorer (ICON) (Immel et al., 2018). The EEJ is an intense band of zonal electric current confined near the magnetic equator flowing in the daytime between ∼90 and 120 km altitude (Yamazaki & Maute, 2017, and references therein). Variations in the EEJ closely track those of the equatorial zonal electric field (i.e., vertical plasma drift) which has widespread effects on the equatorial ionosphere by modifying the production-loss-transport balance. Typically the EEJ flows eastward, associated with an eastward zonal electric field, upward drift, and enhanced equatorial fountain effect, but sometimes the EEJ flows westward, associated with the opposite ionospheric conditions. In the absence of direct solar insolation, the EEJ disappears at night.

ICON and Swarm have been operating simultaneously since ICON's launch in 2019, offering an unprecedented observational capability for studies related to the ionospheric dynamo. On 15 Jan 2022, their orbits were unusually well-synced to provide complementary observations of the Tonga signature, as discussed below. This study does not attempt to quantify properties or classifications of the waves excited by the Tonga explosion, which will undoubtedly be a focus of future investigations. However, the unique opportunity created by coincident observations of the neutral wind by MIGHTI and ionospheric currents by Swarm allows us to directly study the impact of these waves on the ionospheric dynamo, which we report here. In addition, four magnetometer sites are utilized to provide a ground-based perspective on the EEJ variation.

2 Data sources

2.1 ICON-MIGHTI neutral winds

This study uses neutral wind data from the MIGHTI instrument on the ICON spacecraft, which is in a 27° inclination orbit. Neutral wind profiles (ICON data product 2.2 v04) from 90 to 300 km altitude are derived by remote limb observations of the Doppler

shift of naturally occurring green 557.7 nm and red 630.0 nm (OI) airglow emissions. We only use wind data from the dayside, which is when the airglow layers are wide enough to permit wind estimates spanning the full 90 to 300 km altitude range, which fully encompasses the dynamo region. Nightside data have a gap from ∼109 to 210 km. Data are available from the green and red channels with vertical sampling of ∼3 km and ∼10 km, respectively. For this study, to improve statistics especially in regions of dim airglow, we preprocess the green channel by binning vertically by a factor of 2, yielding ∼6 km sampling. Below 180 km altitude, we use samples from the green channel, and above 180 km, we use samples from the red channel. Data above 180 km have a negligible impact on our conclusions regarding the wind dynamo but are included because the volcanogenic waves are clearly evident up to 300 km. The reader is referred to previous publications for more information on the MIGHTI instrument (Englert et al., 2017), processing algorithms (Harding et al., 2017), and on-orbit validation (Harding et al., 2021; Makela et al., 2021).

Although the focus is on two orbits on 15 Jan 2022, we also make use of the entire dataset for background statistics. Specifically, we use all MIGHTI profiles from the start of the mission until 14 Jan 2022 for which the variable "Wind_Quality" is equal to 1 (i.e., highest quality, 1,086,830 profiles in total). To generate these statistics, in addition to the altitude binning discussed above, the data were preprocessed with a 5-sample median filter in time to remove outliers. Data obtained during geomagnetic storms are included in these statistics. Statistics are presented in terms of percentiles; for example, the 90% level for zonal wind represents a value such that 10% of samples have a zonal wind larger than that level.

2.2 Swarm A EEJ current

The Swarm constellation comprises three satellites in near-polar orbits. In this study we use EEJ intensity estimates from one spacecraft, Swarm A, which flies at an altitude of ∼440 km with an inclination of 87.4°. Latitude-dependent height-integrated EEJ intensity is provided by the Swarm Level 2 Product EEF (Eastward Electric Field) (Alken et al., 2013). The EEJ current is estimated from magnetometer measurements during every dayside overflight of the magnetic equator (Alken, 2020). Ground-based validation is discussed by Alken et al. (2015).

In a manner analogous to the wind analysis, background statistics are calculated for context, using the entire available dataset. Specifically, we use the version 0204 dataset spanning 25 Nov 2013 to 14 Jan 2022. We first preprocess the EEJ data to remove non-physical current distributions. These outliers are identified by computing the the total "off-peak current" for each overflight (defined as the root-mean-square of currents poleward of 5 deg quasidipole latitude). Overflights are removed if the off-peak current is larger than 100 times the interquartile range of all the overflights (i.e., 75th percentile minus 25th percentile). This removes 25 overflights which are, by visual inspection, clear non-physical outliers. The 45,184 remaining overflights are used in the statistics below. All data on 15 Jan 2022 remain after this preprocessing step.

2.3 Ground-based magnetometers

We also use ground-based magnetometer data to support the interpretation of the EEJ behavior on 15 Jan 2022. The intensity of the EEJ can be estimated using the horizontal (H) component of the geomagnetic field observed at two stations, one being located at the magnetic equator and the other located about the same longitude but outside the EEJ band (Anderson et al., 2004). The difference in H (ΔH) at the two stations, after subtracting the nighttime baseline, represents the EEJ intensity. We use data from Huancayo (HUA, 12.0°S, 75.3°W) and Piura (PIU, 5.2°S, 80.6°W) for the Peruvian sector, and Tatuoca (TTB, 1.2°S, 48.5°W) and Kourou (KOU, 5.2°N, 52.7°W) for the Brazil-

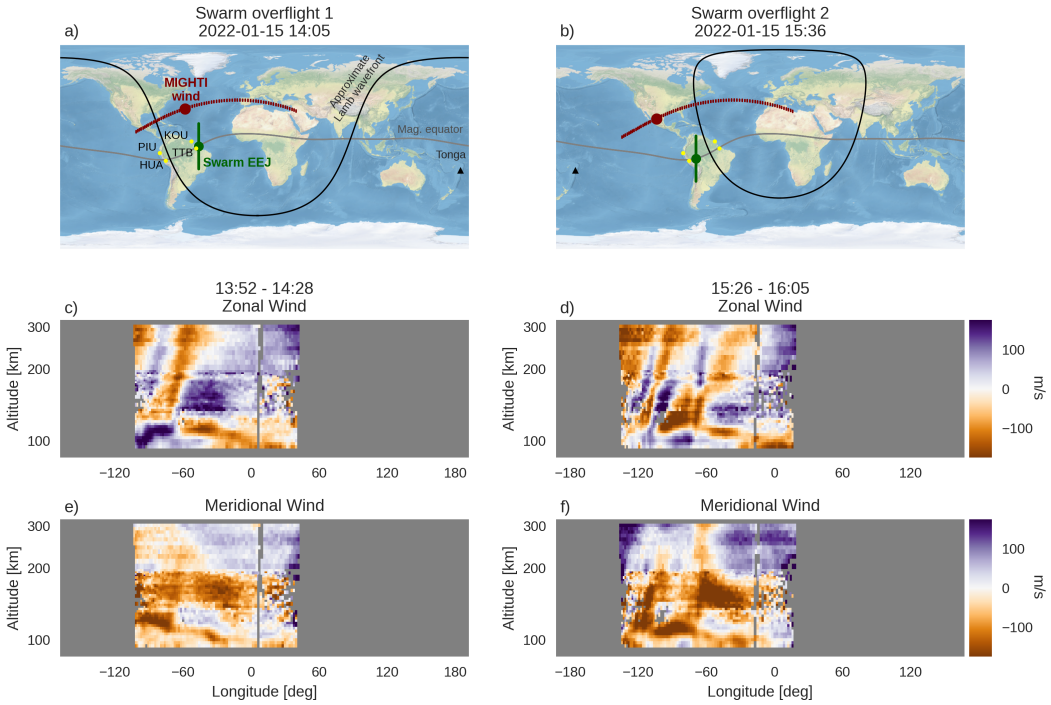

Figure 1. (a,b) Two consecutive orbits of ICON-MIGHTI dayside passes and Swarm equator overflights. The red and green dots indicate the location of the MIGHTI wind observation and Swarm EEJ observation at the respective time. The red and green lines indicate the observation locations just before and after this time. The dashed appearance of the red line denotes individual MIGHTI wind profile locations. The black line indicates the location of a notional radially propagating wavefront moving at 318 m/s that originated in Tonga at 04:28 UT (Wright et al., 2022). Although MIGHTI samples the wind ∼35 degrees farther north than the EEJ, the two sample the same great-circle distance from Tonga with a delay of several minutes. The yellow circles indicate the four ground-based magnetometer sites. (c,d) Daytime zonal wind profiles (positive eastward) measured by MIGHTI corresponding to the longitudes in the map above. Only daytime data are included. The small data gap near 0° longitude is caused by the quality control algorithm masking data when the moon is near the MIGHTI field of view. The altitude axis is in log scale to better display lower thermospheric winds. (e,f) Same as (c,d) for the meridional wind (positive northward).

ian sector. These stations are positioned to detect EEJ signatures in the vicinity of the Swarm observations.

3 Results and Discussion

3.1 Data selection and observational geometry

The Tonga volcanic eruption occurred around 04:15 UT on 15 Jan 2022, near local sunset. Since the tropospheric sound speed is slower than the Earth's rotation at these latitudes, the Lamb wave was mostly contained to the dusk and nighttime sectors for the first several hours after the eruption. In this study we focus on thermosphere-ionosphere signatures once the wave reaches the dayside, where ionospheric currents are strongest. According to the parameters reported by Wright et al. (2022) (318 m/s phase speed orig-

inating in Tonga at 04:28 UT), the lower atmospheric Lamb wave reached the dayside around 13 UT at low/mid-latitudes. Amores et al. (2022) provide further information on the Lamb wave propagation, including a numerical simulation which agrees with the timing used here. The Lamb wave entered the dayside in the American longitude sector. Serendipitously, Swarm A overflights occurred in this sector at 14:05 UT and 15:36 UT. In this study we utilize data from these two orbits and the corresponding orbits of ICON, which samples all longitudes every orbit, albeit at different latitudes.

The two orbits of ICON-MIGHTI data are shown in Figure 1, an animated version of which can be found in the Supporting Information (Movie S1). For context, we show a reference wavefront using the Lamb wave parameters reported by Wright et al. (2022). Given the close alignment between ICON and Swarm, these parameters are not important for our conclusions, and similar parameters (e.g., a 310 m/s wavefront originating at 04:15 UT) do not change the interpretation. On the first orbit (panel a), Swarm A crossed the equator and measured the EEJ at a location roughly 3000 km ahead of the 318 m/s wavefront. At the time Swarm A measured the EEJ at the equator, MIGHTI sampled the wind ∼35 degrees farther north but at a similar great-circle distance from Tonga.

The next orbit is shown to the right (panel b). On this orbit, Swarm A measured the EEJ at a location roughly 1500 km behind the assumed 318 m/s wavefront. At the time of the Swarm A overflight, MIGHTI samples the wind roughly 3500 km behind the wavefront, but reached the same great-circle distance as Swarm A 5 minutes later (15:41 UT).

In both orbits, the MIGHTI data (panels c, d, e, and f) show large wind fluctuations, vertical shears, and coherent wave structures spanning at least 110–300 km, both ahead of and behind the 318 m/s wavefront. Above 120 km, the horizontal wavelengths of the wave structures are estimated by visual inspection to be 3000–5000 km, more than three times as large as the horizontal wavelengths reported in TEC observations in the far field. It is apparent from these observations that the thermospheric signatures of this event are complex and likely not explained by a single wave mode. We do not comment further on the wind features in this paper, but instead we focus on their impact on ionospheric currents in the next section.

In the meridional wind, a discontinuity is evident at 180 km where data from the green and red channels are spliced together. This is a known artifact caused by a drift in the zero-wind reference in the MIGHTI v04 dataset; a new calibration has been implemented and will correct this bias in the next version of the MIGHTI wind dataset. This discontinuity does not affect the qualitative conclusions of this study, which focus on the zonal wind, nor the quantitative calculations in this study, which uses perturbations from the mean, as described below.

3.2 Comparison between MIGHTI winds and Swarm EEJ

Figure 2 compares the Swarm A EEJ observations with the MIGHTI wind observations on these two orbits. On the first orbit (panel a), Swarm A observed an extremely strong eastward EEJ (0.22 A/m). This represents the strongest EEJ observed by Swarm A since 2017, and the 19th strongest overall (stronger than 99.96% of all observations in the Swarm A dataset, which started in 2013). On the next orbit (panel b), Swarm A observes an extreme westward EEJ (-0.17 A/m), often referred to as a counter-electrojet. Except for three overflights during the 22-23 June 2015 geomagnetic storm, this represents the strongest westward EEJ in the Swarm A dataset. Swarm A data from earlier orbits on this day do not show variations above the 90% level. Also shown are statistics computed from all EEJ observations from the start of the mission until 14 Jan 2022. The black line is the median, the dark gray shaded region is the interquartile range (25–75%), and other percentile ranges are shown in lighter gray. Although Swarm B is not included

in this quantitative analysis, data from Swarm B also show a large positive EEJ (0.20 A/m) followed by a large negative EEJ (-0.14 A/m) on these two orbits (not shown). Swarm C flies in a side-by-side configuration to Swarm A, and recorded similar measurements on these two orbits (0.22 A/m and -0.17 A/m respectively, not shown).

The bottom of Figure 2 (panels c and d) shows the MIGHTI zonal winds corresponding to the Swarm A EEJ observations, compared with background variability shown with statistical ranges in gray, analogous to panels a and b. Although the meridional wind fluctuations are in some cases quite significant, we focus on zonal winds because (1) meridional winds are nearly parallel to the magnetic field at the equator and are not expected to strongly influence the EEJ, and (2) the wave is propagating nearly zonally in this region. The dominant large-scale signature of the wave is therefore expected to be in the zonal wind. A separate analysis was conducted where the zonal and meridional winds were combined to calculate the radial wind perturbation in the direction away from Tonga. However, this yielded identical conclusions and was more complicated to compare quantitatively with background statistics.

Zonal wind profiles (shown in red) are chosen such that their distance from Tonga is identical to Swarm A's distance when it crossed the magnetic equator. Insofar as the wave can be assumed to propagate concentrically, this is a proxy for the neutral wind fluctuations in the equatorial region during the Swarm A overflight. The various profiles in Figure 2 are chosen to provide exact alignment for assumed wave velocities ranging from 300 to 330 m/s. The qualitative similarity of these profiles suggests that this procedure to align the Swarm and MIGHTI observations is not significantly sensitive to the assumed wave velocity, a consequence of the fortunate timing of the two observations. The temporal offsets required are 0-4 minutes (overflight 1) and 5-8 minutes (overflight 2), a time scale that is not likely of importance for the large-scale waves observable by MIGHTI. Furthermore, it is the same magnitude as the assumption of temporal persistence used to produce the vector wind estimate by combining the data from the two MIGHTI sensors (5–9 minutes) (Harding et al., 2017). A possibly non-negligible uncertainty in this procedure is the assumption of concentric wave propagation, as the two observations sample along different wave azimuths from Tonga, separated by 5–32 degrees.

These zonal wind profiles are a superposition of the volcanogenic waves and the background thermospheric state upon which they propagate. The black dashed line is an estimate of that background state, computed from an average of profiles at nearly the same local time ($\pm$1 hr) and longitude ($\pm$24 deg, the amount of Earth rotation in one ICON orbit) as the profiles shown. This average is generated using the 4 previous days (Jan 11-14), over which time the sampled latitude changes by no more than 10 deg. It is thus an estimate of the contribution from background migrating and non-migrating tides and planetary waves with periods $\gtrsim$8 days. However, there may also be contributions to the background from short-term tidal variability, short-period planetary waves like the quasi-two-day wave, and geomagnetic activity, which are difficult to comprehensively quantify from a single observatory.

The wind profiles on both orbits are extreme, showing values comparable with, or stronger than, the 0.1% and 99.9% levels. We describe the wind profile in terms of two regions: The "Hall region," ($\sim$100–120 km) where the Hall conductivity is large and dominant, and the "Pedersen region," ($\sim$120–150 km) where the Pedersen conductivity is large and dominant. In reality the Hall and Pedersen conductivities are nonzero over larger altitude ranges, and there is a significant overlap region in which they are both large; however, this description is useful to connect with theoretical arguments below. On orbit 1, when the EEJ is strongly eastward, MIGHTI observes a westward wind in the Hall region, which is not unusual compared to the background profile. However, there is also a strong eastward wind in the Pedersen region which exceeds the 99.9% level. Indeed, this represents the strongest wind observed at $\sim$140 km since the start of the mission. On orbit 2, when the EEJ is strongly westward, MIGHTI observes an eastward wind,

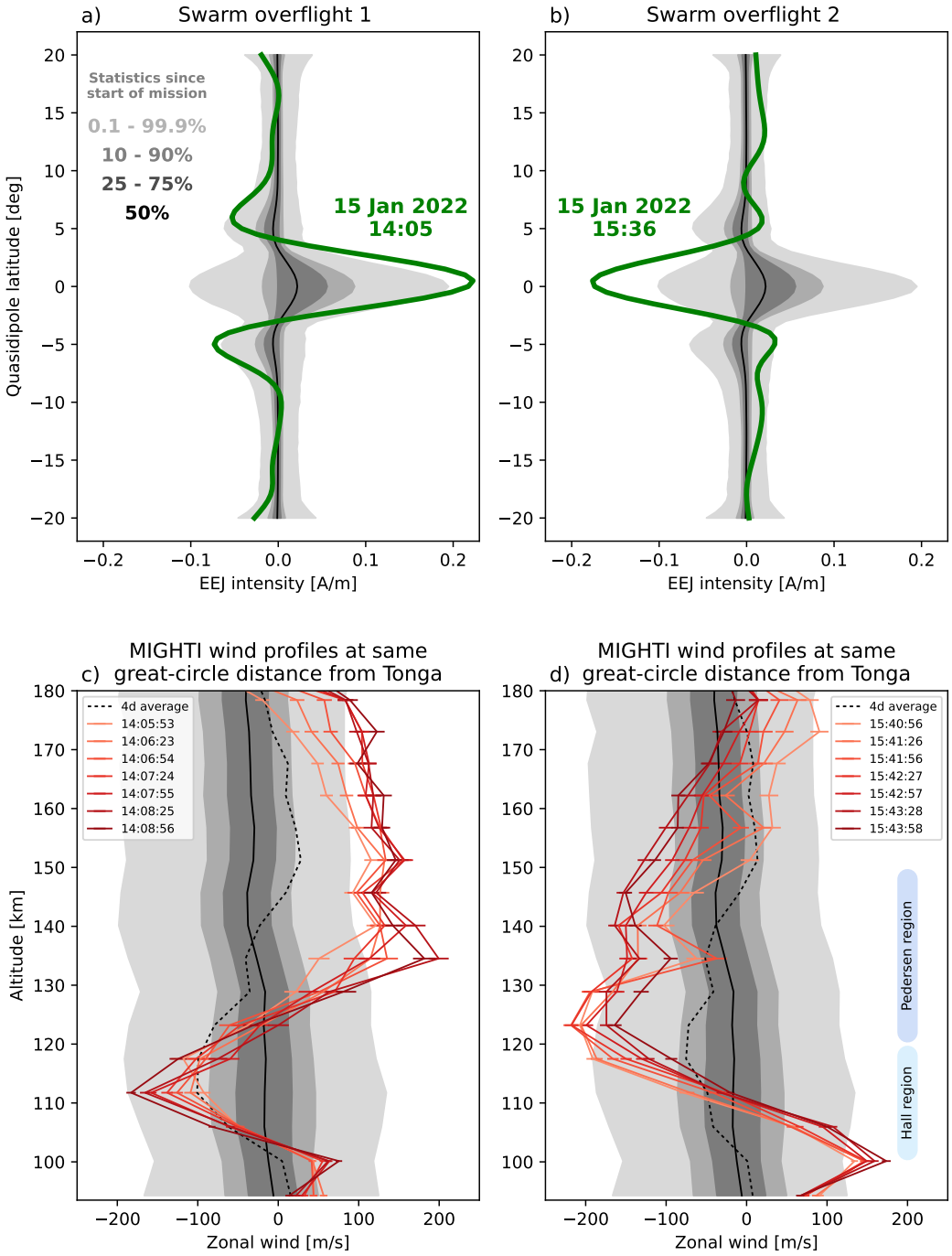

Figure 2. (a,b) Swarm A equatorial electrojet (EEJ) observations during the two orbits shown in Figure 1. (c) MIGHTI wind profiles during the ICON orbit contemporaneous with the Swarm overflight in panel a. (d) Same, except one orbit later, contemporaneous with the Swarm overflight in panel b. Specific wind profiles were chosen to correspond to samples at the same great-circle distance from Tonga as the Swarm observation, for various assumed wave velocities from 300 to 330 m/s. Errorbars represent the uncertainty reported in the v04 wind product, which accounts for shot, read, and dark noise in the detector (i.e., precision). In all 4 panels, the gray shaded areas represent background statistics computed from percentiles of the entire dataset from the start of each mission until 14 Jan 2022, comprising 45,184 Swarm A overflights since 25 Nov 2013 and 1,086,830 MIGHTI profiles since 6 Dec 2019. The black solid line is the median. The black dashed line represents the background wind as computed from four previous days of data at similar local times and longitudes (see text).

peaking around 100 km in the lower Hall region, and a westward wind above ∼110 km, which spans the upper Hall region and the Pedersen region. This profile is unusual relative to the background wind and exceeds the 99.9% level at some altitudes.

This correspondence between the EEJ and neutral winds is consistent with the relationship developed by Yamazaki et al. (2014) and Yamazaki et al. (2021). The early theoretical literature on the EEJ suggested that while height-varying local winds influence the currents outside the EEJ, they are not expected to have a significant influence on the EEJ itself, because it is dominated by the influence of the global zonal electric field (Richmond, 1973). However, the modeling study by Yamazaki et al. (2014) predicted that winds should have a significant role and that the EEJ should be negatively correlated with Hall-region zonal winds and positively correlated with Pedersen-region winds. This was observationally confirmed with the availability of concurrent MIGHTI and Swarm observations by Yamazaki et al. (2021). The implicated mechanism is local generation of electric fields which was not considered explicitly in the early (pre-2000) literature: (1) in the Hall region, an eastward wind drives eastward current, which generates a westward electric field; (2) in the Pedersen region, an eastward wind drives upward current, which generates a downward electric field. At the footpoint of this field line, which lies in the Hall region, the westward currents driven by this electric field will generate an eastward electric field. Since the EEJ current flows in the Hall region, this latter case is a noteworthy example of winds outside the EEJ perturbing currents in the EEJ.

In orbit 1, the strong westward Hall-region wind and strong eastward Pedersen-region wind is expected to cause a strong eastward EEJ through the Yamazaki et al. (2014) relationship. In orbit 2, the Hall-region wind is eastward below 110 km and westward above 110 km, which is expected to yield minimal total forcing in the Hall region. However, the Pedersen-region wind is strongly westward, which is expected to cause a strong westward EEJ. In both cases, the Swarm observations match the expectation. This result confirms the Yamazaki relationship holds under extreme conditions. More interestingly, because the Hall-region effect is small in orbit 2, the EEJ is apparently driven mostly by winds at higher altitudes, confirming the importance of nonlocal wind driving of the EEJ. The current paths that regulate this control deserve further inquiry, both observationally and theoretically.

3.3 Ground-based magnetometer data

In this section we report EEJ observations from two pairs of magnetometers located near the Swarm overflights (see Figure 1). The observations are shown in the first two panels of Figure 3 using blue lines. The black line shows the monthly mean, and the gray shaded area represents 1 standard deviation (i.e., 1σ) above and below the mean.

The HUA-PIU pair in Peru observes a negative ΔH (corresponding to a westward EEJ) beginning around 12 UT, lasting until just after 16 UT (except for one brief period of weak eastward EEJ near 15 UT). The TTB-KOU pair in Brazil observes an eastward EEJ until ∼15 UT, followed by a period of westward EEJ until 18 UT. Superimposed on these broad patterns are shorter, 1-hour scale features which are discussed in the next section.

The broad features and relative timing seen in the magnetometer data are qualitatively consistent with the Swarm observations. Namely, a negative disturbance is first seen over Peru, then over Brazil 2-4 hours later, consistent with eastward propagation. The presence of 1-hour-scale fluctuations and the lack of EEJ before sunrise makes it difficult to estimate the relative timing with greater accuracy. On the first Swarm overflight at 14:05 UT, the nearby Brazilian pair observes an eastward EEJ which is 1σ or less above the climatology. On the second Swarm overflight at 15:36 UT, the Peruvian pair observes a $\sim 2.5\sigma$ extreme westward EEJ. Especially for the positive EEJ on overflight 1, the fluctuations seen by the ground-based magnetometers are not as extreme as the Swarm ob-

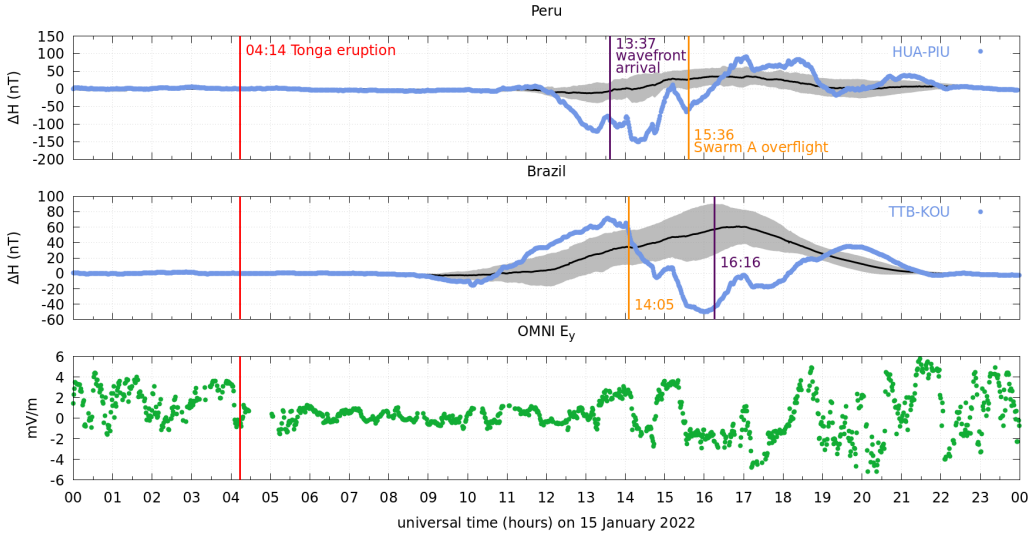

Figure 3. (top) Ground-based magnetometer EEJ intensity estimates over Peru on 15 Jan 2022 computed by subtracting PIU data (off-equator) data from HUA data (on-equator), shown in blue. The monthly mean is in black and ±1 standard deviation range is in gray. The arrival time of a reference 318 m/s Lamb wavefront (purple line) and time of Swarm overflight (yellow line) are also shown. (middle) Same as top, but for Brazil (TTB - KOU). (bottom) Interplanetary eastward electric field from the OMNI database.

servations. Although the cause of this is unknown, it could be due to the ground-based magnetometers being slightly offset from the magnetic equator. In January 2022, TTB and HUA were 2.2° and 0.8° off the magnetic equator according to the CHAOS 7.8 model (Finlay et al., 2020).

The different temporal patterns in Peru and Brazil confirm that the fluctuations observed by Swarm A are not purely spatial but also temporal. The ground-based magnetometer data suggest that the most extreme EEJ activity may have been at locations and times not sampled by Swarm A (e.g., over Brazil at 16 UT). Future work utilizing the global network of magnetometers could help elucidate the evolution of global currents during this event.

The magnetometer data show disturbances before the arrival of the 318 m/s Lamb wavefront (e.g., the negative ΔH in Peru at 13 UT, and the positive and negative ΔH in Brazil before 16 UT). This is consistent with the Swarm A observations ahead of the wavefront at 14:05 UT (Figures 1a and 2a) and the MIGHTI observations on the first orbit (Figure 1c, eastward of -60° longitude). It is likely that the thermospheric response to the eruption is not as simple as the Lamb wave observed in the lower atmosphere, due to the effects of nonlinear evolution, dispersion, self-acceleration, and secondary wave generation, among others. Although no numerical models have yet simulated the upper atmospheric response to the Tonga Lamb wave, Inchin, Heale, et al. (2020) provide a discussion on these processes using a first-principles model of the thermospheric signature of tsunamis.

3.4 Geomagnetic storm effects

A moderate geomagnetic storm began on 14 Jan 2022; the Tonga eruption and subsequent wave propagation occurred during the recovery phase. It is thus important to distinguish the signatures caused by the Tonga eruption from the effects of the storm.

The EEJ is known to be modified by electric fields penetrating from the magnetosphere and electric fields originating from the stormtime disturbance dynamo (Yamazaki & Maute, 2017, and references therein). First, we rule out penetration electric field effects.

Figure 3 (bottom panel) shows the interplanetary electric field (IEF) y-component (dawn-to-dusk electric field) from OMNI data (King & Papitashvili, 2005). The data are taken directly from the OMNI database, except they include a 17-minute delay to account for the delay between the bowshock and the ionosphere (Manoj et al., 2008). If the penetration electric field were the main cause of the EEJ variations, we would expect to see strong correlations between the IEF and ΔH in both longitude sectors. Quantitatively, the Pearson correlations between IEF and the deviations of ΔH from the monthly mean, (blue lines minus solid black lines in Figure 3), between 8 and 16 hr local time is -0.02 for Peru (13 to 22 UT) and 0.35 for Brazil (11 to 20 UT). However, the fluctuations observed in IEF appear to correlate with 1-hour-scale fluctuations observed at both ground-based sites simultaneously (e.g., positive excursions at 15 UT and 17 UT, and possibly at 13.5 UT). After filtering ΔH and IEF to remove their 100-minute running mean, the correlation increased to 0.60 (Peru) and 0.61 (Brazil). Thus, it is likely that the 1-hour-scale fluctuations are caused in part by the penetration electric field, but the larger, longer perturbations of interest here are not. Because of this, and because of the consistency between the EEJ signatures and the neutral wind signatures, as discussed above, we rule out the penetration electric field as the main cause of the extreme eastward and westward EEJ observed by Swarm.

With neutral winds established as the causative mechanism, it is important to rule out geomagnetic activity as the cause of the extreme winds seen in Figure 2(c,d). It is well known that the EEJ can be reversed by the disturbance dynamo, a consequence of westward Coriolis forcing of neutral winds accelerated equatorward by auroral heating (Yamazaki & Maute, 2017). According to the modeling study by Huang et al. (2005), disturbance winds caused by a geomagnetic storm are mainly in the westward direction at middle and low latitudes. MIGHTI observations show both eastward and westward wind perturbations, which are different from the predicted pattern of the disturbance winds. Also, storm-driven wind perturbations are predicted to be much greater at F-region heights (above 150 km) than at E-region heights (below 150 km). MIGHTI observations show large wind perturbations below 150 km (including an eastward perturbation at 100 km exceeding 100 m/s), which does not fit the classical picture of the disturbance winds. Furthermore, the westward disturbance wind at mid and low latitudes is stronger during nighttime than daytime. For instance, Xiong et al. (2015) showed that the average westward disturbance wind at 20–50° latitude is less than 50 m/s for Kp>4 at F-region heights during daytime, while it can exceed 100 m/s during nighttime. Thus, the geomagnetic storm is unlikely to be the main cause of the extreme daytime winds detected by MIGHTI.

The simultaneous occurrence of the Lamb wave arrival, the EEJ signal, and the wind signal, combined with the lack of any significant wind or EEJ signals before this time, represents strong evidence to attribute the observed fluctuations to disturbances caused by the Tonga eruption. Nevertheless, it is possible that high-latitude heating launched traveling atmospheric disturbances during the recovery phase, and it is likely that the longer-term circulation changes caused by the storm have changed the background conditions upon which the Tonga signal is superimposed. It will be an interesting topic for future modeling and observational studies to elucidate the interplay of geomagnetic storm and volcanogenic effects on the thermosphere and ionosphere during this period.

4 Conclusion

The 15 Jan 2022 Tonga volcanic eruption caused extreme fluctuations in the ionospheric wind dynamo, as observed by Swarm and ICON. On the leading part of the ini-

tial disturbance, Swarm A observed an extreme (0.22 A/m) eastward EEJ at the 99.96th percentile of typical variability, while ICON-MIGHTI observed a strong westward wind in the Hall region and a strong eastward wind in the Pedersen region, a relationship consistent with recent theoretical and observational studies. Relative to typical variability, the wind perturbations (up to 200 m/s) were at or above the 99.9th percentile, and at some altitudes (e.g., ∼140 km) were the strongest observed since ICON's launch. On the trailing part of the initial disturbance, Swarm A observed the strongest westward EEJ (-0.17 A/m) of the mission, except for the 22-23 June 2015 geomagnetic storm, while ICON-MIGHTI observed eastward and westward winds in the Hall region and a westward wind in the Pedersen region, also at or above the 99.9th percentile.

The relationship between winds and EEJ is consistent with the theoretical and observational relationships of neutral wind driving developed by Yamazaki et al. (2014) and Yamazaki et al. (2021). The westward electrojet in this case appears to be driven mostly by westward winds in the Pedersen region. Since the EEJ flows in the Hall region, this is a noteworthy example of nonlocal wind driving of the EEJ. The energy and current paths involved in this relationship would be an interesting topic for further study.

Initial reports on the global ionosphere-thermosphere impacts of the Tonga eruption have focused on small- and meso-scale (300–1000 km wavelength) waves seen in TEC at amplitudes of at most a few TEC units, as well as geomagnetic fluctuations 835 km away from and soon after the eruption. The MIGHTI and Swarm observations suggest that modifications of the ionospheric dynamo were extreme relative to background variability, even after ∼10 hours and ∼10,000 km of wave propagation. This is expected to have caused significant and observable redistributions of ionospheric plasma. As an example of an enormous impulse function, the Tonga eruption may be a useful test for atmosphere-ionosphere coupled models in extreme cases, and the neutral wind and EEJ current signatures reported here could be useful targets.

Acknowledgments

The authors would like to recognize the work of the ICON and Swarm engineering and science teams. ICON is supported by NASA's Explorers Program through contracts NNG12FA45C and NNG12FA42I. The results presented in this paper rely on magnetic observatory data collected at Huancayo (HUA), Piura (PIU), Kourou (KOU), and Tatuoca (TTB). We thank the Instituto Geofísico del Perú (HUA, PIU), Bureau Central de Magnétisme Terrestre at the Institut de Physique du Globe de Paris (KOU), Observatório Nacional (TTB) and GFZ German Research Centre for Geosciences (TTB) for supporting the operations of these observatories and INTERMAGNET for promoting high standards of magnetic observatory practice (www.intermagnet.org). The authors thank Hermann Lühr, Claudia Stolle, Eileen McIver, and Jonathan Makela for fruitful scientific discussions and suggestions.

Open Research

ICON data can be retrieved from the ICON website (`https://icon.ssl.berkeley.edu/Data`). The European Space Agency (ESA) is gratefully acknowledged for providing Swarm data, which is available from the Swarm website (`https://swarm-diss.eo.esa.int/#swarm%2FLevel2daily%2FEntire_mission_data%2FEEF%2FTMS%2FSat_A`). The OMNI data were obtained from the GSFC/SPDF OMNIWeb interface at `https://omniweb.gsfc.nasa.gov`. Ground-based magnetometer data from HUA, TTB, and KOU are available from `https://intermagnet.org/data-donnee/download-eng.php`. Data from PIU is available from the LISN network (`http://lisn.igp.gob.pe/jdata/view/magnetometer/minute/piur/?itype=magnetometer&dtype=minute&daterange=2022%2F01%2F15+-+2022%2F01%2F15&networks=on&N_IGP=on&N_LISN=on&N_MAGDAS=on&countries=on&C_Argentina=on&C_Brasil=on&C_Colombia=on&C_Peru=on&stations=on&S_areq=`

458 on&S_leon=on&S_cuib=on&S_dejp=on&S_huan=on&S_jica=on&S_ancm=on&S_huam=on&S
459 _icam=on&S_nazc=on&S_piur=on&bt_view=piur&S_saol=on&S_tara=on).

460 References

461 Aa, E., Zhang, S.-R., Erickson, P. J., Vierinen, J., Coster, A. J., Goncharenko, L. P.,
462 ... Rideout, W. (2022). Significant equatorial plasma bubbles and global
463 ionospheric disturbances after the 2022 tonga volcano eruption. *Earth and*
464 *Space Science Open Archive*, 17. Retrieved from https://doi.org/10.1002/
465 essoar.10510637.1 doi: 10.1002/essoar.10510637.1
466 Adam, D. (2022). Tonga volcano eruption created puzzling ripples in Earth's at-
467 mosphere. *Nature*, *601*, 497. Retrieved from https://www.nature.com/
468 articles/d41586-022-00127-1 doi: 10.1038/d41586-022-00127-1
469 Alken, P. (2020). Estimating currents and electric fields at low latitudes from
470 satellite magnetic measurements. In M. W. Dunlop & H. Lühr (Eds.), *Iono-*
471 *spheric multi-spacecraft analysis tools: Approaches for deriving ionospheric*
472 *parameters* (pp. 233–254). Cham: Springer International Publishing. Re-
473 trieved from https://doi.org/10.1007/978-3-030-26732-2_11 doi:
474 10.1007/978-3-030-26732-2_11
475 Alken, P., Maus, S., Chulliat, A., Vigneron, P., Sirol, O., & Hulot, G. (2015). Swarm
476 equatorial electric field chain: First results. *Geophysical Research Letters*,
477 *42*(3), 673–680. doi: 10.1002/2014GL062658
478 Alken, P., Maus, S., Vigneron, P., Sirol, O., & Hulot, G. (2013). Swarm SCARF
479 equatorial electric field inversion chain. *Earth, Planets and Space*, *65*(11),
480 1309–1317. doi: 10.5047/eps.2013.09.008
481 Amores, A., Monserrat, S., Marcos, M., Argüeso, D., Villalonga, J., Jordà, G., &
482 Gomis, D. (2022). Numerical simulation of atmospheric Lamb waves generated
483 by the 2022 Hunga-Tonga volcanic eruption. *Geophysical Research Letters*,
484 1–8. doi: 10.1029/2022gl098240
485 Anderson, D., Anghel, A., Chau, J., & Veliz, O. (2004). Daytime vertical E × B
486 drift velocities inferred from ground-based magnetometer observations at low
487 latitudes . *Space Weather*, *2*(11), n/a-n/a. doi: 10.1029/2004sw000095
488 Aryal, S., Evans, J. S., Correira, J., Burns, A. G., Wang, W., Solomon, S. C., ...
489 Jee, G. (2020). First Global-Scale Synoptic Imaging of Solar Eclipse Effects in
490 the Thermosphere. *Journal of Geophysical Research: Space Physics*, *125*(9).
491 doi: 10.1029/2020JA027789
492 Astafyeva, E. (2019). Ionospheric Detection of Natural Hazards. *Reviews of Geo-*
493 *physics*, *57*(4), 1265–1288. doi: 10.1029/2019RG000668
494 Bretherton, F. P. (1969). Lamb waves in a nearly isothermal atmosphere. *Quarterly*
495 *Journal of the Royal Meteorological Society*, *95*(406), 754–757. Retrieved from
496 https://onlinelibrary.wiley.com/doi/10.1002/qj.49709540608 doi: 10
497 .1002/qj.49709540608
498 Englert, C. R., Harlander, J. M., Brown, C. M., Marr, K. D., Miller, I. J., Stump,
499 J. E., ... Immel, T. J. (2017). Michelson Interferometer for Global High-
500 Resolution Thermospheric Imaging (MIGHTI): Instrument Design and Cali-
501 bration. *Space Science Reviews*, *212*(1-2), 553–584. Retrieved from http://
502 dx.doi.org/10.1007/s11214-017-0358-4http://link.springer.com/
503 10.1007/s11214-017-0358-4 doi: 10.1007/s11214-017-0358-4
504 Finlay, C. C., Kloss, C., Olsen, N., Hammer, M. D., Tøffner-Clausen, L., Grayver,
505 A., & Kuvshinov, A. (2020). The CHAOS-7 geomagnetic field model and
506 observed changes in the South Atlantic Anomaly. *Earth, Planets and Space*,
507 *72*(1), 1–31.
508 Garrett, C. J. (1969). Atmospheric edge waves. *Quarterly Journal of the Royal Me-*
509 *teorological Society*, *95*(406), 731–753. doi: 10.1002/qj.49709540607
510 Harding, B. J., Chau, J. L., He, M., Englert, C. R., Harlander, J. M., Marr, K. D.,

... Immel, T. J. (2021). Validation of ICON-MIGHTI Thermospheric Wind Observations: 2. Green-Line Comparisons to Specular Meteor Radars. *Journal of Geophysical Research: Space Physics*, *126*(3), 1–12. Retrieved from https://onlinelibrary.wiley.com/doi/10.1029/2020JA028947 doi: 10.1029/2020JA028947

Harding, B. J., Makela, J. J., Englert, C. R., Marr, K. D., Harlander, J. M., England, S. L., & Immel, T. J. (2017). The MIGHTI Wind Retrieval Algorithm: Description and Verification. *Space Science Reviews*, *212*(1-2), 585–600. Retrieved from http://dx.doi.org/10.1007/s11214-017-0359-3http://link.springer.com/10.1007/s11214-017-0359-3 doi: 10.1007/s11214-017-0359-3

Huang, C.-M., Richmond, A., & Chen, M.-Q. (2005). Theoretical effects of geomagnetic activity on low-latitude ionospheric electric fields. *Journal of Geophysical Research: Space Physics*, *110*(A5).

Immel, T. J., England, S. L., Mende, S. B., Heelis, R. A., Englert, C. R., Edelstein, J., ... Sirk, M. M. (2018). The Ionospheric Connection Explorer Mission: Mission Goals and Design. *Space Science Reviews*, *214*(1), 13. Retrieved from http://dx.doi.org/10.1007/s11214-017-0449-2http://link.springer.com/10.1007/s11214-017-0449-2 doi: 10.1007/s11214-017-0449-2

Inchin, P. A., Heale, C. J., Snively, J. B., & Zettergren, M. D. (2020). The Dynamics of Nonlinear Atmospheric Acoustic-Gravity Waves Generated by Tsunamis Over Realistic Bathymetry. *Journal of Geophysical Research: Space Physics*, *125*(12), 1–18. doi: 10.1029/2020JA028309

Inchin, P. A., Snively, J. B., Zettergren, M. D., Komjathy, A., Verkhoglyadova, O. P., & Tulasi Ram, S. (2020). Modeling of Ionospheric Responses to Atmospheric Acoustic and Gravity Waves Driven by the 2015 Nepal Mw7.8 Gorkha Earthquake. *Journal of Geophysical Research: Space Physics*, *125*(4). doi: 10.1029/2019JA027200

King, J. H., & Papitashvili, N. E. (2005). Solar wind spatial scales in and comparisons of hourly Wind and ACE plasma and magnetic field data. *Journal of Geophysical Research: Space Physics*, *110*(A2), 1–9. doi: 10.1029/2004JA010649

Li, R., Lei, J., & Dang, T. (2021). The Solar Eclipse Effects on the Upper Thermosphere. *Geophysical Research Letters*, *48*(15), 1–10. doi: 10.1029/2021GL094749

Lin, J.-T., Rajesh, P. K., Lin, C. C. H., Chou, M.-Y., Liu, J.-Y., Yue, J., ... Kung, M.-M. (2022). Rapid conjugate appearance of the giant ionospheric lamb wave in the northern hemisphere after hunga-tonga volcano eruptions. *Earth and Space Science Open Archive*, 27. Retrieved from https://doi.org/10.1002/essoar.10510440.2 doi: 10.1002/essoar.10510440.2

Makela, J. J., Baughman, M., Navarro, L. A., Harding, B. J., Englert, C. R., Harlander, J. M., ... Immel, T. J. (2021). Validation of ICON-MIGHTI Thermospheric Wind Observations: 1. Nighttime Red-Line Ground-Based Fabry-Perot Interferometers. *Journal of Geophysical Research: Space Physics*, *126*(2), 1–29. Retrieved from https://onlinelibrary.wiley.com/doi/10.1029/2020JA028726 doi: 10.1029/2020JA028726

Manoj, C., Maus, S., Lühr, H., & Alken, P. (2008). Penetration characteristics of the interplanetary electric field to the daytime equatorial ionosphere. *Journal of Geophysical Research: Space Physics*, *113*(12), 1–11. doi: 10.1029/2008JA013381

Nishida, K., Kobayashi, N., & Fukao, Y. (2014). Background Lamb waves in the Earth's atmosphere. *Geophysical Journal International*, *196*(1), 312–316. Retrieved from https://academic.oup.com/gji/article/196/1/312/594635 doi: 10.1093/gji/ggt413

Richmond, A. D. (1973). Equatorial electrojet-I. Development of a model including

winds and instabilities. *Journal of Atmospheric and Terrestrial Physics*, *35*(6), 1083–1103. doi: 10.1016/0021-9169(73)90007-X

Soares, G., Yamazaki, Y., & Matzka, J. (2022). Localized geomagnetic disturbance due to ionospheric response to the hunga tonga eruption on january 15, 2022. *Earth and Space Science Open Archive*, 12. Retrieved from `https://doi.org/10.1002/essoar.10510482.1` doi: 10.1002/essoar.10510482.1

Themens, D. R., Watson, C., Žagar, N., Vasylkevych, S., Elvidge, S., McCaffrey, A., ... Jayachandran, P. (2022). Global propagation of ionospheric disturbances associated with the 2022 Tonga Volcanic Eruption. *Geophysical Research Letters*. doi: 10.1029/2022gl098158

Wright, C., Hindley, N., Alexander, M. J., Barlow, M., Hoffmann, L., Mitchell, C., ... et al. (2022). Tonga eruption triggered waves propagating globally from surface to edge of space. *Earth and Space Science Open Archive*, 23. Retrieved from `https://doi.org/10.1002/essoar.10510674.1` doi: 10.1002/essoar.10510674.1

Xiong, C., Lühr, H., & Fejer, B. G. (2015). Global features of the disturbance winds during storm time deduced from CHAMP observations. *Journal of Geophysical Research A: Space Physics*, *120*(6), 5137–5150. doi: 10.1002/2015JA021302

Yamazaki, Y., Harding, B. J., Stolle, C., & Matzka, J. (2021). Neutral Wind Profiles During Periods of Eastward and Westward Equatorial Electrojet. *Geophysical Research Letters*, *48*(11), 1–10. doi: 10.1029/2021GL093567

Yamazaki, Y., & Maute, A. (2017). Sq and EEJ—A Review on the Daily Variation of the Geomagnetic Field Caused by Ionospheric Dynamo Currents. *Space Science Reviews*, *206*(1-4), 299–405. Retrieved from `http://dx.doi.org/10.1007/s11214-016-0282-z` doi: 10.1007/s11214-016-0282-z

Yamazaki, Y., Richmond, A. D., Maute, A., Liu, H.-L., Pedatella, N., & Sassi, F. (2014). On the day-to-day variation of the equatorial electrojet during quiet periods. *Journal of Geophysical Research: Space Physics*, *119*(8), 6966–6980. Retrieved from `http://doi.wiley.com/10.1002/2014JA020243` doi: 10.1002/2014JA020243

Zettergren, M. D., & Snively, J. B. (2019). Latitude and Longitude Dependence of Ionospheric TEC and Magnetic Perturbations From Infrasonic-Acoustic Waves Generated by Strong Seismic Events. *Geophysical Research Letters*, *46*(3), 1132–1140. doi: 10.1029/2018GL081569

Zhang, S.-r., Vierinen, J., Aa, E., & Goncharenko, L. P. (2022). 2022 Tonga volcanic eruption induced global propagation of ionospheric disturbances via Lamb waves. *Frontiers in Astronomy and Space Sciences*, *9*, 1–15. doi: 10.3389/fspas.2022.871275